



Cite this: *React. Chem. Eng.*, 2017, 2, 168

Structural and kinetic changes to small-pore Cu-zeolites after hydrothermal aging treatments and selective catalytic reduction of NO_x with ammonia†

Jonatan D. Albarracin-Caballero,^{‡a} Ishant Khurana,^{‡a} John R. Di Iorio,^a Arthur J. Shih,^a Joel E. Schmidt,^b Michiel Dusselier,^{bc} Mark E. Davis,^b Aleksey Yezerets,^d Jeffrey T. Miller,^a Fabio H. Ribeiro^{*a} and Rajamani Gounder^{*a}

Three small-pore, eight-membered ring (8-MR) zeolites of different cage-based topology (CHA, AEI, RTH), in their proton- and copper-exchanged forms, were first exposed to high temperature hydrothermal aging treatments (1073 K, 16 h, 10% (v/v) H₂O) and then to reaction conditions for low temperature (473 K) standard selective catalytic reduction (SCR) of NO_x with ammonia, in order to study the effect of zeolite topology on the structural and kinetic changes that occur to Cu-zeolites used in NO_x abatement. UV-visible spectra were collected to monitor changes to Cu structure and showed that band intensities for isolated, hydrated Cu²⁺ cations (~12500 cm⁻¹) remain constant after hydrothermal aging, but decrease in intensity upon subsequent exposure to low temperature SCR reaction conditions. Standard SCR rates (per Cu, 473 K), activation energies, and reaction orders are similar between Cu-AEI and Cu-CHA zeolites before and after hydrothermal aging, although rates are lower after hydrothermal aging as expected from the decreases in intensity of UV-visible bands for Cu²⁺ active sites. For Cu-RTH, rates are lower (by 2–3×) and apparent activation energies are lower (by ~2×) than for Cu-AEI or Cu-CHA. These findings suggest that the RTH framework imposes internal transport restrictions, effectively functioning as a one-dimensional framework during SCR catalysis. Hydrothermal aging of Cu-RTH results in complete deactivation and undetectable SCR rates, despite X-ray diffraction patterns and Ar micropore volumes (87 K) that remain unchanged after hydrothermal aging treatments and subsequent SCR exposure. These findings highlight some of the differences in low temperature SCR behavior among small-pore Cu-zeolites of different topology, and the beneficial properties conferred by double six-membered ring (D6R) composite building units. They demonstrate that deleterious structural changes to Cu sites occur after exposure to hydrothermal aging conditions and SCR reactants at low temperatures, likely reflecting the formation of inactive copper-aluminate domains. Therefore, the viability of Cu-zeolites for practical low temperature NO_x SCR catalysis cannot be inferred solely from assessments of framework structural integrity after hydrothermal aging treatments, but also require Cu active site and kinetic characterization after hydrothermally aged zeolites are exposed to low temperature SCR reaction conditions.

Received 1st November 2016,
Accepted 7th December 2016

DOI: 10.1039/c6re00198j

rsc.li/reaction-engineering

^a Charles D. Davidson School of Chemical Engineering, Purdue University, 480 Stadium Mall Drive, West Lafayette, IN 47907, USA. E-mail: fabio@purdue.edu, rgounder@purdue.edu

^b Chemical Engineering, California Institute of Technology, 1200 E. California Boulevard, MC 210-41, Pasadena, CA 91125, USA

^c Center for Surface Chemistry and Catalysis, KU Leuven, Celestijnenlaan 200F, 3001 Heverlee, Belgium

^d Cummins Inc., 1900 McKinley Ave., MC 50183, Columbus, IN 47201, USA

† Electronic supplementary information (ESI) available. See DOI: 10.1039/c6re00198j

‡ J. D. A.-C. and I. K. contributed equally to this work.

1. Introduction

Leading emissions control strategies for the abatement of hazardous nitrogen oxide pollutants (NO_x, x = 1, 2) in lean-burn and diesel engine exhaust involve their selective catalytic reduction (SCR) with ammonia, which is generated from the decomposition of urea stored in an on-board tank. Cu- and Fe-exchanged molecular sieves used to practice automotive SCR aftertreatment^{1–6} are required to retain sufficient SCR performance after excursions to high temperatures (>923 K) in the presence of steam (~7% H₂O (v/v)),^{7–10} conditions experienced during regeneration of particulate filters. The

structural integrity of molecular sieve frameworks with medium pores (e.g., MFI,^{11–16} FER;¹¹ ~0.5 nm diam.) and large pores (e.g., BEA,^{13,14,17,18} FAU;¹⁴ >0.6 nm diam.) becomes compromised during hydrothermal aging;^{11–18} moreover, active sites within such frameworks can be poisoned chemically by residual hydrocarbons in exhaust streams. These deactivation issues are mitigated within small-pore, eight-membered ring (8-MR; <0.4 nm diam.) frameworks, which led to the advent of the aluminosilicate (SSZ-13) and silicoaluminophosphate (SAPO-34) compositions of the chabazite (CHA) topology^{8,19,20} as commercially used NO_x SCR catalysts. Other small-pore molecular sieves with three-dimensional (e.g., AFX,¹³ AEI,²¹ KFI,¹³ SAV,²² SFW^{23,24}) and two-dimensional (e.g., LEV,¹³ DDR,¹³ RTH²⁵) pore connectivity have been considered as alternatives to CHA molecular sieves, based on observations that small-pore frameworks retain their structural integrity after exposure to hydrothermal aging conditions.

Hydrothermal aging of zeolites leads to the removal of aluminum atoms from framework locations,^{13,26–28} which stabilize redox-active, extraframework Cu cations and ammonium species during SCR catalysis. Framework dealumination generally leads to sintering of extraframework alumina and mixed oxide domains with concomitant losses in microporous structure^{29–31} that may restrict molecular traffic to active sites. The effects of hydrothermal aging treatments on dealumination have been assessed by changes in Al coordination using solid-state ²⁷Al magic angle spinning nuclear magnetic resonance (MAS NMR), and in long-range crystalline structure using X-ray diffraction (XRD) and micropore volume measurements.^{14,32–35} Structural changes upon dealumination are more severe in Cu-exchanged medium-pore and large-pore zeolites (e.g., Cu-MFI, Cu-BEA) than in small-pore zeolites (e.g., Cu-CHA, Cu-AEI),^{14,17,36} which are more recalcitrant to hydrothermal deactivation. Aluminum hydroxide species (Al(OH)₃; ~0.5 nm in diam.) formed upon dealumination at high temperatures are thought to be unable to diffuse through 8-MR windows in CHA¹³ and AEI³⁶ (~0.38 nm in diam.), which prevents the formation of larger extraframework alumina aggregates and allows for reincorporation of monomeric Al species within framework vacancy positions at low temperatures. Dealumination upon hydrothermal aging is also suppressed by the presence of extraframework cations (e.g., Cu, Na, Li, Mg),^{36–38} which remove Brønsted acid sites that are vulnerable locations for hydrolysis of framework bonds.^{39–41} Consequently, the ability of a zeolite framework to resist dealumination and retain its structural integrity upon hydrothermal aging has been used to identify promising candidates for practical NO_x SCR catalysis.

Deactivation caused by hydrothermal aging of molecular sieves may also reflect changes to the structure and location of extraframework Cu cations, such as their aggregation into larger Cu oxide species (Cu_xO_y), because the former isolated cations have been implicated as active sites for low temperature (473 K) SCR catalysis^{42–44} while the latter oxide clusters are unreactive.⁴⁵ The disappearance of isolated Cu²⁺ cations

upon hydrothermal aging of Cu-SSZ-13 has been inferred from the attenuation of absorption features characteristic of framework (T–O–T) vibrations (900 and 940 cm⁻¹) perturbed by ion-exchanged Cu species in diffuse-reflectance infrared (DRIFTS) spectra, from decreases in the amount of NH₃ desorbed from Lewis acidic Cu cations (~553 K) in TPD experiments,³² and from decreases in electron paramagnetic resonance (EPR) signals for isolated Cu²⁺ cations.³³ The aggregation of isolated Cu²⁺ cations into larger Cu_xO_y domains upon hydrothermal aging has been detected by electron microscopy (TEM, SEM) and energy dispersive X-ray spectroscopy (EDX).^{32–34} Isolated Cu²⁺ cations have also been proposed to interact with extraframework Al species, formed *via* dealumination, to generate inactive copper-aluminate domains in hydrothermally aged Cu-SSZ-13, evident in extended X-ray absorption fine structure (EXAFS) spectra that show decreased Cu–Cu scattering distances and increased Cu–Al scattering distances, and in H₂ temperature programmed reduction (TPR) profiles that show decreased intensities of lower temperature (500–670 K) reduction features for isolated Cu cations with the concomitant appearance of higher temperature (790–880 K) reduction features attributed to copper-aluminates.³⁵ Additionally, ²⁷Al MAS NMR spectra show decreased intensities for tetrahedral Al lines ($\delta \sim 60$ ppm) without concomitant increases in intensities for octahedral Al lines ($\delta \sim 0$ ppm), suggesting that interactions of Al with paramagnetic Cu render them invisible to NMR detection.¹⁴ These results provide evidence for one possible deactivation mechanism of Cu-SSZ-13 through loss of isolated Cu²⁺ active sites during hydrothermal aging, but do not account for structural changes to active sites that may result from subsequent exposure to standard SCR reactants. Thus, identifying new zeolite topologies that retain SCR reactivity after hydrothermal aging treatments requires knowledge of how such treatments, and subsequent exposure to SCR reaction conditions, affect the structures of both Cu active sites and the zeolite framework.

Here, we investigate the effects of hydrothermal aging and subsequent exposure to standard SCR reactants at low temperatures (473 K) on the structural and active site changes experienced by three different small-pore Cu-exchanged zeolites (Cu-CHA, Cu-AEI, Cu-RTH). Bulk characterization techniques, including XRD patterns and micropore volumes, reveal only subtle differences between Cu-zeolites before and after hydrothermal aging, and after subsequent exposure to low temperature SCR reaction conditions, and are unable to provide direct insight into the decreases in SCR reactivity measured on hydrothermally aged, small-pore Cu-zeolites. We provide evidence that exposure of hydrothermally aged catalysts to SCR reaction conditions at low temperatures causes further structural changes to active Cu sites that are detectable by UV-visible spectroscopy, consistent with the formation of mixed copper-aluminate domains *via* reaction with extraframework Al species formed upon dealumination during hydrothermal aging. These findings demonstrate that active site and structural characterization of hydrothermally aged Cu-zeolites

after exposure to SCR reactants at low temperatures provide more accurate inferences about their catalytic behavior.

2. Experimental methods

2.1. Catalyst synthesis and treatment

A sample of CHA (SSZ-13) zeolite with a Si/Al ratio of 15 was made as reported elsewhere.⁴⁶ Briefly, 28.4 g of *N,N,N*-trimethyl-1-adamantylammonium hydroxide (TMAdaOH, Sachem, 25 wt%) were mixed with 71.4 g of deionized water (18.2 MΩ), 0.87 g of aluminum hydroxide (SPI Pharma, 99.9 wt%, 0325 grade), and 34.6 g of 0.1 M sodium hydroxide (NaOH; Alfa Aesar), then stirred for 15 minutes at ambient conditions. 10 g of fumed silica (Cab-o-Sil M-5) were added to the mixture and stirred for 2 hours at ambient conditions. The final molar composition of the synthesis solution was $1\text{SiO}_2/0.033\text{Al}_2\text{O}_3/0.20\text{TMAdaOH}/0.02\text{NaOH}/23.8\text{H}_2\text{O}$. All reagents were used without further purification. The resulting solution was transferred to eight Teflon-lined Parr autoclaves (45 mL each) and held at 433 K for 10 days under rotation.

A sample of AEI (SSZ-39) zeolite with a Si/Al ratio of 9.5 was synthesized in a rotating oven at 413 K for 4 days as reported elsewhere,⁴⁷ using *cis*-2,6-dimethylpiperidinium hydroxide as the organic structure directing agent (OSDA). The molar composition of the synthesis mixture was $1\text{SiO}_2/0.017\text{Al}_2\text{O}_3/0.07\text{OSDA}/0.65\text{OH}^-/0.58\text{Na}^+/12.3\text{H}_2\text{O}$, obtained by mixing (aqueous) OSDA, NaOH (1 M, RT Baker), double distilled water, sodium silicate (N® type, PQ Corporation) and CBV500 (NH₄-USY, Si/Al = 2.6, Zeolyst). A sample of RTH (SSZ-50) zeolite with a Si/Al ratio of 15 was made using the CBV720 synthesis protocol reported elsewhere.^{48–50}

As-synthesized zeolites were washed alternately with deionized water and acetone, recovered *via* centrifugation, and dried at 323 K for 24 hours. The dried samples were then treated to 873 K (0.0083 K s⁻¹) in air (Commercial grade, Indiana Oxygen) for 6 hours before ion-exchanging in an aqueous 0.1 M NH₄NO₃ solution (Sigma Aldrich; 1000 mL per g zeolite) at 353 K for 10 hours. NH₄-exchanged zeolites were washed with deionized H₂O, recovered *via* centrifugation, dried at 323 K for 24 hours, then treated at 823 K (0.0083 K s⁻¹) in air for 6 hours to obtain H-form zeolites. Cu-exchanged CHA, AEI, and RTH zeolites were prepared *via* liquid phase ion-exchange of H-form zeolites using an aqueous 0.2 M Cu(NO₃)₂ solution (99.999% trace metals basis, Sigma-Aldrich; 150 mL per g zeolite) at ambient temperature for 4 hours. The pH during the exchange was not controlled and the final pH of the solution was ~3.6.

Hydrothermal aging experiments were performed on Cu-zeolites in a three-zone horizontal tube furnace (Applied Test Systems Series 3210), in which each zone was equipped with independent temperature control (Watlow EZ-Zone PM Express). Once the furnace temperature reached 373 K, water was introduced *via* syringe pump (KD Scientific Legato 100) into a stream of flowing air (100 mL min⁻¹, 99.999%, Indiana Oxygen), which was transferred to the furnace through stainless steel lines held at >373 K. Approximately 1 gram of cata-

lyst was loaded into quartz boats held within the tube furnace and treated to 1073 K (0.033 K s⁻¹) for 16 hours in flowing air (100 mL min⁻¹, 99.999%, Indiana Oxygen) containing 10% (v/v) water. After treatment for 16 hours at 1073 K, water was removed from the flowing air stream while the sample was cooled to ambient.

2.2. Catalyst structural characterization

Powder diffraction patterns were collected using a Rigaku SmartLab diffractometer with a Cu Kα radiation source (1.76 kW), from 4 to 40° with a scan rate of 0.05° s⁻¹ and a step size of 0.01°. Diffraction patterns are normalized so that the maximum peak intensity in each pattern is unity. The diffraction patterns were compared to reference patterns to confirm the RTH, CHA and AEI topologies.⁵¹

Ar adsorption isotherms were used to determine micropore volumes on zeolite samples (87 K) using a Micromeritics ASAP 2020 Surface Area and Porosity Analyzer. Micropore volumes were obtained by converting adsorbed gas volumes (cm³ g_{cat}⁻¹ at STP) to liquid volumes assuming the liquid density of Ar at 87 K. Samples were pelleted and sieved to retain particles between 125–250 μm in diameter. Samples (0.03–0.05 g) were degassed by heating to 393 K (0.167 K s⁻¹) under high vacuum (~5 μm Hg) for 2 h, and then heating to 623 K (0.167 K s⁻¹) under high vacuum (~5 μm Hg) and holding for 9 h. Micropore volumes (cm³ g_{cat}⁻¹ at STP) were estimated from extrapolation of the linear volumetric uptake during the beginning of mesopore filling (~0.08–0.30 *P/P*₀) to zero relative pressure, which agreed with micropore volumes estimated from analyzing the semi-log derivative plot of the adsorption isotherm ($\partial(V_{\text{ads}})/\partial(\ln(P/P_0))$ vs. $\ln(P/P_0)$).

In order to quantify the fractions of framework and extraframework Al, ²⁷Al magic angle spinning nuclear magnetic resonance (MAS NMR) spectra were recorded on H-form and Cu-form CHA, AEI and RTH zeolite samples. NMR spectra were collected using a Chemagnetics CMX-Infinity 400 spectrometer in a wide-bore 9.4 Tesla magnet (Purdue Interdepartmental NMR Facility) and were acquired at ambient conditions using a 2.3 μs pulse (equivalent to *ca.* 30 degrees), an acquisition time of 12.8 ms and a relaxation delay of 1 s, and were measured at 104.24 MHz and a MAS rate of 5 kHz. ¹H decoupling was used during acquisition, employing two-pulse phase modulation (TPPM) scheme. Prior to packing in a 4 mm ZrO₂ rotor, zeolite samples were hydrated by holding for >48 h in a desiccator containing a saturated potassium chloride (KCl) solution. All ²⁷Al MAS NMR spectra are referenced to a static sample of AlCl₃ dissolved in D₂O (0 ppm ²⁷Al line).

Diffuse reflectance UV-visible spectra were recorded under ambient conditions using a Varian UV-vis-NIR spectrophotometer (Cary 5000) with a diffuse reflectance accessory consisting of two ellipsoidal mirrors (Harrick Scientific Praying Mantis). Barium sulfate (BaSO₄, 99.9%, Sigma-Aldrich) was used as the 100% reflectance standard. An *ex situ* sample holder was loaded with 0.1 g of sample, which was

pelleted and sieved to retain particles between 125–250 μm in diameter. Spectra were collected from 7000 to 50 000 cm^{-1} with a scan speed of 2000 $\text{cm}^{-1} \text{min}^{-1}$, and spectra of the H-form zeolite was subtracted from those for corresponding Cu-zeolites to correct for contributions of absorption from the framework.

2.3. Brønsted acid site quantification using NH_3 titration methods

The total number of Brønsted acid sites (H^+) on H-form and Cu-exchanged zeolites was quantified by temperature programmed desorption (TPD) of NH_3 on a gas-phase plug flow reactor, as described by Bates *et al.*,⁵² using a procedure described elsewhere.⁵³ For H-form zeolites, NH_3 saturation was performed *via* aqueous-phase exchange with NH_4^+ cations, as reported elsewhere.⁵² For Cu-exchanged zeolites, samples were saturated with 500 ppm NH_3 diluted with He (99.999%, UHP, Indiana Oxygen) at 433 K for 2 h with a total flow rate of 350 mL min^{-1} . Following this NH_3 saturation step, the sample was flushed with 2.5–3.0% water in UHP He (wet purge) at 433 K for 8 h while maintaining the same total flow rate to desorb NH_3 bound to non-protonic sites. Following the wet purge step, samples were heated to 820 K (0.167 K s^{-1}) under flowing He (UHP, 350 mL min^{-1}). The total moles of NH_3 desorbed during the TPD experiment was measured using on-board calibrations in an MKS Multigas 2030 gas-phase FT-IR spectrometer.⁵²

2.4. Kinetic measurements of standard SCR turnover rates

Standard selective catalytic reduction (SCR) kinetics were measured on a bench-top tubular glass reactor described elsewhere.⁵² All samples were sieved to a nominal size of 125–250 μm and diluted with silica gel to obtain a bed height of ~ 2.5 cm. Steady-state kinetic data were collected at NO conversions below 20% (differential); thus, the entire catalyst bed was exposed to approximately the same gas concentrations. Under standard SCR conditions, the reactant gas mixture comprised 300 ppm NO (3.6% NO/Ar, Praxair), 300 ppm NH_3 (3.0% NH_3/Ar , Praxair), 7% CO_2 (liquid, Indiana Oxygen), 10% O_2 (99.5%, Indiana Oxygen), 2.5% H_2O (deionized, 18.2 $\text{M}\Omega$, introduced through saturator), and balance N_2 (99.999% UHP, Indiana Oxygen). For all kinetic measurements, the total gas stream was maintained at a flow rate of 1.5 L min^{-1} and at ambient pressure (~ 101 kPa). Apparent reaction orders were measured by independently varying partial pressures of NH_3 (0.02–0.05 kPa), NO (0.02–0.05 kPa) or O_2 (5–15 kPa) in the reactant gas stream, and adjusting the balance N_2 to maintain a constant total gas flow rate and pressure. Apparent activation energies were measured under standard SCR conditions by varying the temperature between 444–476 K. Outlet gas concentrations were analyzed using on-board gas calibrations on an MKS MultigasTM 2030 gas-phase Fourier transform infrared (FTIR) spectrometer and NO, NO_2 , NH_3 , CO_2 , and H_2O concentration data was recorded every 0.95 s. Kinetic measurements were recorded

after waiting for outlet gas concentrations to reach steady-state, which typically occurred after 2–4 hours. Reactant pressures and temperatures were then varied over the course of 18 hours, and finally returned to initial conditions to verify that catalytic rates returned to their initial steady-state values and that the catalyst had not undergone any deactivation.

3. Results and discussion

3.1. Structural features of CHA, AEI and RTH topologies

The salient structural features of the three molecular sieve framework topologies studied here are summarized in Table 1. The CHA framework⁴⁶ has three-dimensional micro-pore interconnectivity and is formed by the repetitive stacking of a hexagonal array of planar 6-membered rings (6-MR) connected in an AABCC-type stacking scheme that form hexagonal prisms (double 6-MR). These double 6-MR (D6R) units are ordered to form large chabazite cages that are ~ 0.73 nm in diameter, which are limited by symmetric 8-MR windows that are ~ 0.38 nm in diameter. The CHA framework contains only one crystallographically unique T-site and its unit cell contains 36 tetrahedrally-coordinated atoms (T-atoms) connected by 4-MR, 6-MR, and 8-MR units that are shared between adjacent cages.

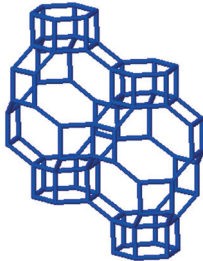
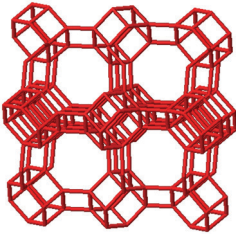
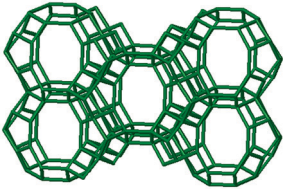
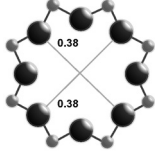
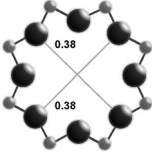
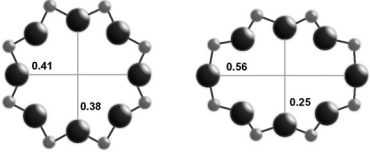
The AEI framework⁵⁴ also has three-dimensional micro-pore interconnectivity and is constructed from a hexagonal array of 6-MR units similar to CHA, but neighboring D6R units are rotated 180° with respect to each other (Table 1). The D6R units are ordered to form AEI cavities that are ~ 0.73 nm in diameter and are contained within 4-MR, 6-MR, and 8-MR units, with access into AEI cavities limited by symmetric 8-MR windows that are ~ 0.38 nm in diameter, as in the case of CHA. In contrast to the CHA unit cell, the AEI unit cell contains 48 T-atoms and three crystallographically-distinct T-sites.

The RTH framework⁵⁵ is unique among the three small-pore zeolites studied here because it does not contain D6R building units, but instead is formed by two sets of three 4-MR that are connected *via* 5-MR linkages. These chained 4-MR and 5-MR periodic building units are repeated with simple translations to form RTH cavities that are 0.81 nm in diameter, and are contained within 4-MR, 5-MR, 6-MR, and 8-MR units. Consequently, the RTH unit cell (32 T-atoms) contains both symmetric (0.38 nm \times 0.41 nm) and asymmetric (0.25 nm \times 0.56 nm) 8-MR windows that result in only two-dimensional pore interconnectivity. RTH contains four crystallographically-distinct T-sites, three of which occupy positions accessible through either of the two 8-MR windows, and one that resides within the interconnected 4-MR chain and is inaccessible from the RTH cavity.

3.2. Synthesis and characterization of H-form and Cu-form zeolites before hydrothermal aging

Powder XRD patterns of H-form AEI, CHA, and RTH zeolites (Fig. S.1, ESI[†]) were consistent with reported diffraction

Table 1 Structural properties of the 8-MR molecular sieve frameworks in this study (CHA, AEI, RTH)

| Framework | CHA | AEI | RTH |
|---------------------------------------|---|--|---|
| Crystal topology |  |  |  |
| |  |  |  |
| Zeolite trade name | SSZ-13 (ref. 46) | SSZ-39 (ref. 54) | SSZ-50 (ref. 55) |
| Space group | $R\bar{3}m$ | $Cmcm$ | $C2/m$ |
| Ring sizes (X-MR) ^a | 8, 6, 4 | 8, 6, 4 | 8, 6, 5, 4 |
| Number of unique T-sites ^a | 1 | 3 | 4 |
| Connectivity ^a | 3-D | 3-D | 2-D |
| Window diameter ^b (nm) | 0.38 × 0.38 | 0.38 × 0.38 | 0.54 × 0.25 0.41 × 0.38 |
| Cage diameter ^c (nm) | 0.73 | 0.73 | 0.81 |

^a Structural information from the International Zeolite Association structural database.⁵¹ ^b Window diameter taken as the maximum diameter of a sphere that can diffuse through the framework.⁶⁸ ^c Cage size taken as the maximum diameter of a sphere that be occluded within the framework.⁶⁸

patterns for these topologies⁵¹ and did not show diffraction peaks for phase impurities. Ar adsorption isotherms (87 K) on H-form zeolites (Fig. S.2, ESI[†]) gave micropore volumes (Table 2) consistent with the AEI,⁵⁴ CHA,⁴⁶ and RTH⁵⁵ topologies. ²⁷Al MAS NMR spectra of H-form zeolites (Fig. S.3.1–S.3.3, ESI[†]) show predominantly Al incorporated into tetrahedral framework positions (Al_f , $\delta \sim 60$ ppm), with Al_f/Al_{tot} values quantified to be 0.85 for H-CHA, 0.85 for H-AEI and 0.94 for H-RTH (Table 2). The number of protons per framework Al atom (H^+/Al_f , Table 2) measured by NH_3 TPD (Fig. 2) on H-form zeolites was 0.95 and 0.85 for H-CHA and H-AEI, respectively, indicating that nearly every framework Al generated a proton. In contrast, the H^+/Al_f value was much lower on H-RTH (0.60, Table 2), suggesting either that some framework Al atoms generate H^+ sites that

are inaccessible to NH_3 , or that not all Al atoms are associated with a corresponding proton site. In the RTH framework, it is plausible that some H^+ sites are inaccessible to NH_3 , which has a kinetic diameter (~ 0.26 nm)⁵⁶ that is larger than one of the dimensions of the distorted RTH window (0.56 nm × 0.25 nm), and because one of the four T-sites in RTH is in a location that is inaccessible from the RTH cage. Infrared spectra collected after H-RTH was exposed to NH_3 (433 K), however, showed complete disappearance of Brønsted acidic OH stretches (Fig. S.4, ESI[†]) indicating that all H^+ sites are accessible to NH_3 . Therefore, the H^+/Al_f value of 0.60 on H-RTH reflects the presence of distorted Al structures that do not generate H^+ sites, but are otherwise detected as Al_f species in NMR spectra, as noted previously.^{45,57,58}

Table 2 Site and structural properties of H-form and Cu-form zeolites prior to hydrothermal aging

| Sample | Si/Al ratio ^a | Cu ^a wt% | Cu/Al ratio ^a | $V_{ads,micro}^b$ (cm ³ g ⁻¹) | $V_{ads,meso}^b$ (cm ³ g ⁻¹) | H^+/Al ratio ^c | Al_f/Al_{tot}^d | H^+/Al_f |
|--------|--------------------------|---------------------|--------------------------|--|---|-----------------------------|-------------------|------------|
| H-CHA | 15 | — | — | 0.18 | 0.04 | 0.95 | 0.85 | 1.10 |
| Cu-CHA | 15 | 0.7 | 0.12 | 0.17 | 0.05 | 0.72 | 0.90 | — |
| H-AEI | 9.5 | — | — | 0.20 | 0.01 | 0.85 | 0.85 | 1.00 |
| Cu-AEI | 9.5 | 1.7 | 0.17 | 0.19 | 0.01 | 0.54 | 0.91 | — |
| H-RTH | 15 | — | — | 0.20 | 0.05 | 0.60 | 0.94 | 0.61 |
| Cu-RTH | 15 | 0.7 | 0.11 | 0.17 | 0.04 | 0.38 | 0.98 | — |

^a Elemental composition determined by atomic absorption spectroscopy (AAS). ^b Micropore and mesopore volumes determined from Ar adsorption isotherms (87 K) (Fig. S.2, ESI). ^c Number of H^+ sites quantified by selective NH_3 titration and temperature-programmed desorption.

^d Fraction of tetrahedrally coordinated Al determined from ²⁷Al MAS NMR (Fig. S.3.1–S.3.3, ESI).

Powder XRD patterns of AEI, CHA, and RTH zeolites after Cu exchange do not show significant changes in structure compared to their respective H-form zeolites or the presence of bulk Cu_xO_y (Fig. S.1, ESI†). The micropore volume of each Cu-exchanged zeolite decreased slightly (Table 2; Fig. S.2, ESI†) due to the presence of extraframework Cu cations, which occupy a small, but detectable, fraction of the void volume. Gaseous NH_3 titration^{53,59} of residual H^+ sites on Cu-CHA (Cu/Al = 0.12) shows that H^+ sites are replaced with an exchange stoichiometry of two protons per Cu, reflecting the presence of only divalent Cu^{2+} cations (Table 2, Fig. 2). This result is consistent (within experimental error) with the sequential exchange of isolated Cu^{2+} at paired Al sites until saturation followed by subsequent exchange of monovalent $[\text{CuOH}]^+$ at isolated Al sites.^{42,60,61} Cu-RTH (Cu/Al = 0.11) shows an H^+/Cu exchange stoichiometry of two that suggests only Cu^{2+} sites are present, while Cu-AEI (Cu/Al = 0.17) shows an H^+/Cu exchange stoichiometry between 1 and 2 that suggests a mixture of Cu^{2+} and $[\text{CuOH}]^+$ sites are present. UV-visible spectra of hydrated Cu-AEI, Cu-CHA, and Cu-RTH zeolites (Fig. 3) show absorption bands characteristic of d-d transitions for hydrated Cu^{2+} complexes ($\sim 12\,500\text{ cm}^{-1}$) and broad bands for metal-ligand charge transfer ($35\,000\text{--}47\,000\text{ cm}^{-1}$), which are convoluted by zeolitic framework metal-oxygen charge transfer ($36\,750$ and $43\,500\text{ cm}^{-1}$) and Cu-O charge transfer ($\sim 42\,000\text{ cm}^{-1}$).^{62–64} An additional feature is present at $\sim 25\,000\text{ cm}^{-1}$ in the UV-vis spectrum of Cu-RTH, but not in spectra of either Cu-AEI or Cu-CHA, and appears in a region attributed to Cu-O charge transfer in small Cu oxide clusters.⁶³

3.3. Standard SCR kinetics of Cu-zeolites before hydrothermal aging

Rates of NO consumption (473 K, per Cu) during standard SCR (equimolar NO and NH_3 , with O_2 as the oxidant) are shown in Table 3 and plotted in Fig. 4. The measured NO consumption rate (per Cu) was similar on Cu-AEI and Cu-CHA (within 1.3 \times), although direct quantitative comparison of these turnover rates is not rigorously justified since they appear to be measured in different kinetic regimes, reflected in the different apparent NH_3 reaction orders of -0.5 and -0.1 on Cu-CHA and Cu-AEI (Table 3), respectively. The measured NO consumption rate was lower (by 2.2–2.9 \times) on Cu-RTH than on either Cu-AEI or Cu-CHA (Table 3). At first glance, the similar turnover rates (per Cu) on Cu-CHA, Cu-AEI and Cu-RTH (within 3 \times , 473 K) seem reminiscent of standard SCR turnover rates (473 K) that have been reported to be insensitive to the zeolite topology (CHA, BEA, MFI), as a consequence of the solvation of Cu cations by NH_3 during low temperature SCR conditions.⁴²

Apparent activation energies (Table 3) estimated from rate data collected between 444–476 K (Fig. 4) were similar on Cu-AEI ($46 \pm 5\text{ kJ mol}^{-1}$) and Cu-CHA ($56 \pm 5\text{ kJ mol}^{-1}$), and in a range previously reported for standard SCR activation energies on Cu-CHA (Si/Al = 35, Cu/Al = 0–0.31).^{44,45} Apparent activation energies were much lower on Cu-RTH ($28 \pm 5\text{ kJ mol}^{-1}$), however, and approximately half of the value measured on Cu-CHA, characteristic of severe intrazeolite mass transfer limitations. Both the CHA and AEI frameworks contain three-dimensional pore systems interconnected by

Table 3 Site and structural properties of H-form zeolites, and of Cu-exchanged zeolites before and after hydrothermal aging, and before and after exposure to standard SCR gases. Standard SCR rates (473 K), apparent activation energies, and apparent reaction orders for Cu-form zeolites before and after hydrothermal aging treatments

| Sample | Exposure to SCR gases | $V_{\text{ads,micro}}^a$ ($\text{cm}^3\text{ g}^{-1}$) | $V_{\text{ads,meso}}^a$ ($\text{cm}^3\text{ g}^{-1}$) | $\text{H}^+/\text{Al}_{\text{tot}}$ ratio ^b | $\text{Al}_f/\text{Al}_{\text{tot}}$ | Standard SCR rate (per total Cu, 473 K) ^c | E_{app}^d (kJ mol^{-1}) | NO order ^e | O_2 order ^e | NH_3 order ^e |
|--------------|-----------------------|---|--|---|--------------------------------------|---|--|--------------------------|------------------------------------|-------------------------------------|
| CHA | | | | | | | | | | |
| H-Form | | 0.18 | 0.04 | 0.95 | 0.85 | | | | | |
| Cu-Form | Before | 0.17 | 0.05 | 0.72 | 0.90 | | | | | |
| | After | 0.17 | 0.03 | 0.70 | | 3.1 | 56 ± 5 | 0.4 | 0.6 | -0.5 |
| Cu-Form aged | Before | 0.15 | 0.01 | 0.16 | 0.84 | | | | | |
| | After | 0.15 | 0.07 | 0.14 | | 2.2 | 51 ± 5 | 0.5 | 0.4 | -0.1 |
| AEI | | | | | | | | | | |
| H-Form | | 0.20 | 0.01 | 0.85 | 0.85 | | | | | |
| Cu-Form | Before | 0.19 | 0.01 | 0.54 | 0.91 | | | | | |
| | After | 0.18 | 0.00 | 0.50 | | 4.1 | 46 ± 5 | 0.5 | 0.4 | -0.1 |
| Cu-Form aged | Before | 0.17 | 0.06 | 0.16 | 0.78 | | | | | |
| | After | 0.16 | 0.02 | 0.15 | | 1.9 | 49 ± 5 | 0.5 | 0.4 | 0.0 |
| RTH | | | | | | | | | | |
| H-Form | | 0.20 | 0.05 | 0.60 | 0.94 | | | | | |
| Cu-Form | Before | 0.17 | 0.04 | 0.38 | 0.98 | | | | | |
| | After | 0.17 | 0.03 | 0.39 | | 1.4 | 28 ± 5 | 0.4 | 0.4 | -0.1 |
| Cu-form aged | Before | 0.17 | 0.10 | 0.07 | 0.72 | | | | | |
| | After | 0.17 | 0.08 | 0.00 | | n.d.* | — | — | — | — |

^a Micropore and mesopore volumes determined from Ar adsorption isotherms (87 K) (Fig. 6). ^b Number of H^+ sites quantified by selective NH_3 titration and temperature-programmed desorption. ^c Units of $10^{-3}\text{ mol NO (mol Cu)}^{-1}\text{ s}^{-1}$. ^d Errors $\pm 7\text{ kJ mol}^{-1}$. ^e Errors are ± 0.1 . *n.d., not detectable ($<0.3 \times 10^{-3}\text{ mol NO (mol Cu)}^{-1}\text{ s}^{-1}$).

symmetric 8-MR windows (0.38 nm diameter), but the RTH framework is a two-dimensional pore system with a limiting asymmetric 8-MR ring of size (0.25 nm) similar to the kinetic diameter of the SCR reactants (~ 0.3 nm). In effect, the RTH framework appears to behave as a one-dimensional pore system for this reaction, in which reactants preferentially diffuse through the symmetric 8-MR window. Internal diffusion limitations have been proposed to account for the lower NO_x conversions (423–573 K) in two-dimensional, small-pore LEV and DDR zeolites, when compared to three-dimensional small-pore CHA zeolites.¹³ Thus, while small-pore zeolites show improved hydrothermal stability over medium and large-pore zeolites,^{14,17} considerations of pore connectivity and limiting aperture sizes are also critical in determining the reactivity of Cu sites located within them.

The number of residual H^+ sites (per Al_{tot}) on Cu-CHA before and after exposure to SCR gases was 0.72 and 0.70 ± 0.05 , respectively. Similarly, the residual H^+/Al_f value on Cu-AEI and Cu-RTH changed only from 0.54 to 0.50 ± 0.05 and from 0.38 to 0.39 ± 0.05 , respectively (Table 3). Therefore, exposure to SCR gases did not significantly change the number of residual H^+ sites on Cu-AEI, Cu-CHA and Cu-RTH, indicating that framework Al remained largely intact on Cu-zeolites after NO_x SCR catalysis. Ar micropore and mesopore volume measurements (87 K) on Cu-AEI, Cu-CHA and Cu-RTH before and after exposure to SCR gases were unchanged (Table 3, Fig. 6), with micropore volumes for both Cu-CHA and Cu-RTH of $0.17 \text{ cm}^3 \text{ g}^{-1}$ and for Cu-AEI of $0.18\text{--}0.19 \text{ cm}^3 \text{ g}^{-1}$ before and after exposure to SCR gases, respectively. Similarly, the mesopore volume for Cu-AEI, Cu-CHA and Cu-RTH zeolites before and after exposure to SCR gases were the same, within experimental error, between $0.03\text{--}0.05 \text{ cm}^3 \text{ g}^{-1}$ (Table 3). Taken together, these characterization data of Cu-zeolites that have not been exposed to hydrothermal aging treatments indicate that minimal changes to H^+ or Cu sites, or the zeolite framework, occur after exposure to low temperature standard SCR reaction conditions (473 K).

3.4. Characterization of Cu-form zeolites before and after hydrothermal aging

Severe hydrothermal aging treatments of each Cu-exchanged zeolite, performed to reproduce the effects experienced during a 135 000 mile lifetime (1073 K, 10% (v/v) H_2O , 16 h),³⁴ did not result in detectable loss of long-range structure as inferred from powder XRD patterns (Fig. 5). After hydrothermal aging treatments, the Ar micropore volumes decreased by only $\sim 10\%$ on Cu-AEI and Cu-CHA, but remained constant on Cu-RTH (Table 3, Fig. 6). ^{27}Al MAS NMR spectra of Cu-zeolites after hydrothermal aging (Fig. 1) show decreased intensities for tetrahedrally-coordinated Al lines (Al_f , ~ 60 ppm; Table 3) and increased intensities in octahedrally-coordinated Al lines (Al_{ex} , ~ 0 ppm; Fig. 1), indicating the formation of extraframework Al species from framework dealumination. Framework dealumination occurred to greater extents on Cu-RTH ($\sim 25\%$ loss in Al_f) than on either

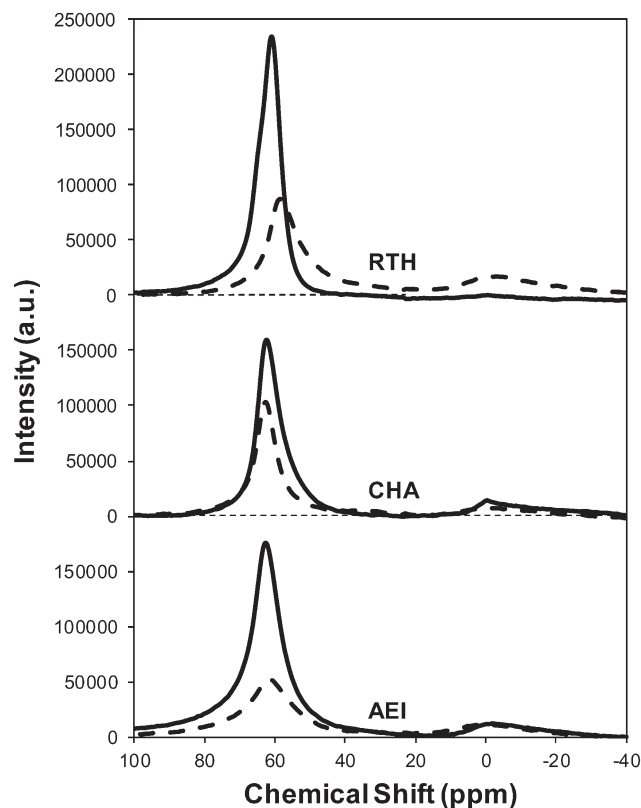


Fig. 1 ^{27}Al MAS NMR spectra of hydrated fresh (solid) and aged (dashed) Cu-form of RTH, CHA and AEI zeolites.

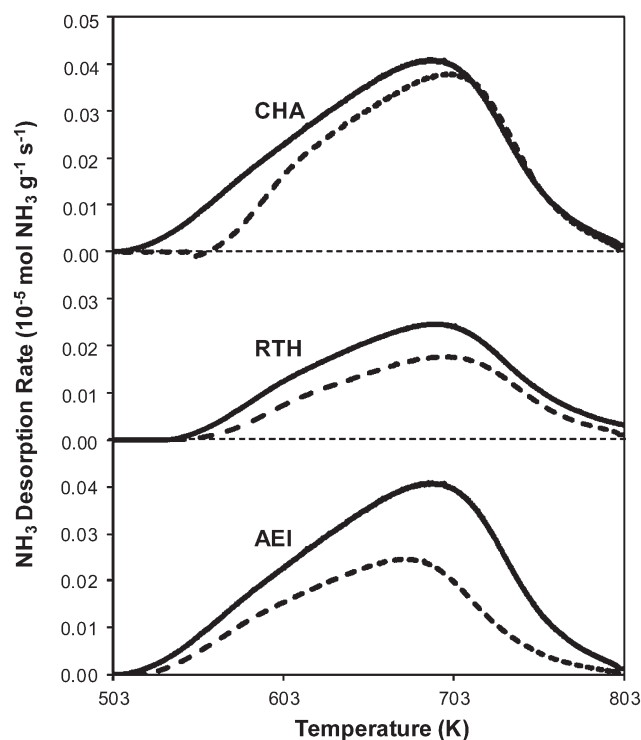


Fig. 2 NH_3 desorption rates as a function of temperature on H-form (solid) and fresh Cu-form (dashed) on AEI, CHA, and RTH zeolites.

Cu-AEI or Cu-CHA ($\sim 7\%$ loss in Al_f), although we note that Al quantification from NMR spectra of Cu-zeolites will be affected by species that are not detected because of interactions with paramagnetic Cu. Moreover, hydrothermal aging of Cu-RTH results in the appearance of a broad shoulder at $\sim 40\text{--}50$ ppm reflecting penta-coordinated or distorted tetrahedral Al,⁶⁵ which did not occur in either Cu-AEI or Cu-CHA. After hydrothermal aging treatments, XRD lines shifted to higher angles on Cu-CHA and Cu-AEI (Fig. 5) reflecting lattice contraction upon extraction of a small amount of framework Al ($\sim 7\%$ by ^{27}Al NMR), while XRD lines shifted to lower angles on Cu-RTH (Fig. 5) reflecting lattice expansion that appears to arise from the more extensive dealumination that formed persistent partial-extraframework aluminum species in distorted coordination environments ($\sim 40\text{--}50$ ppm in ^{27}Al NMR). After hydrothermal aging, each Cu-zeolite sample showed a $\sim 70\text{--}80\%$ decrease in the number of H^+ sites measured by NH_3 TPD (Table 3; Fig. S.5, ESI[†]), in spite of the only minor decreases in Al_f intensity observed in the ^{27}Al MAS NMR spectra, which may reflect structural changes to extraframework Al species caused by the hydration treatments used prior to recording NMR spectra. These findings demonstrate that characterization of the bulk structure (e.g. XRD patterns, micropore volumes) or Al atoms (^{27}Al MAS NMR) are insufficient to describe the local site and structural changes caused by hydrothermal aging treatments,³⁶ and serve as a reminder for the need to use techniques that probe and quantify active sites directly (e.g. base titration of proton sites) to accurately detect such structural changes.^{59,66,67}

In contrast to the dramatic changes observed for H^+ sites on each Cu-zeolite after hydrothermal aging, the identity and coordination of Cu species appear to remain unchanged as inferred from UV-vis spectra (Fig. 3). UV-vis absorption bands for Cu^{2+} d-d transitions ($\sim 12\,500\text{ cm}^{-1}$) appear identical for hydrated Cu-zeolites before and after hydrothermal aging, without any new features observed in the region for Cu oxide clusters ($\sim 25\,000\text{ cm}^{-1}$). Slight changes in the intensities of absorbance bands characteristic of metal-ligand charge transfer ($35\,000\text{--}47\,000\text{ cm}^{-1}$) are observed for each Cu-zeolite after hydrothermal aging, which may reflect changes in the zeolite structure caused by removal of framework aluminum atoms. Taken together, these results indicate that hydrothermal aging treatments of Cu-exchanged CHA, AEI and RTH zeolites cause framework dealumination and a decrease in the numbers of corresponding H^+ sites, but do not result in detectable changes to the exchanged Cu cations or to the long-range structural order in the zeolite framework.

3.5. Standard SCR kinetics of Cu-form zeolites before and after hydrothermal aging

The standard SCR rate (per Cu, 473 K) measured on hydrothermally aged Cu-AEI decreased by $\sim 50\%$ compared to the rate measured on Cu-AEI prior to aging (Table 3, Fig. 4). The standard SCR rate measured on hydrothermally aged Cu-CHA decreased by $\sim 25\%$ compared to the rate measured on Cu-

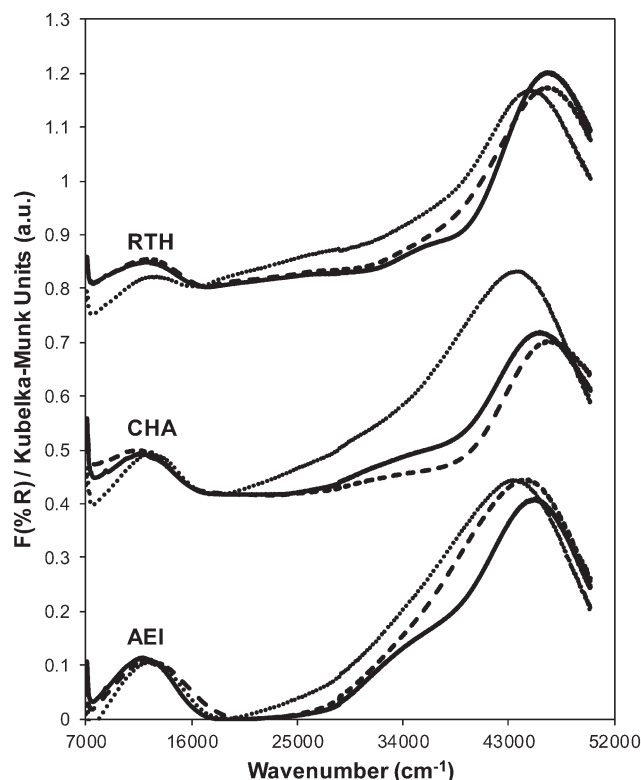


Fig. 3 UV-vis spectra on hydrated fresh Cu-form before SCR (solid), aged Cu-form before SCR (dashed), and aged after SCR (dotted) on RTH, CHA and AEI zeolites. Spectra are offset for clarity (CHA: by 0.4 a.u., RTH: by 0.8 a.u.).

CHA prior to aging (Table 3, Fig. 4). The standard SCR rate on Cu-RTH, however, was not measurable ($<0.3 \times 10^{-3}$ mol NO (mol Cu) $^{-1}$ s $^{-1}$) after hydrothermal aging despite the presence of isolated, hydrated Cu^{2+} species detected in its UV-vis spectrum (Fig. 3). As a result, apparent activation energies and reaction orders could not be measured on Cu-RTH subjected to hydrothermal aging treatments. Although hydrothermally aged Cu-RTH shows undetectable SCR rates, XRD patterns and Ar micropore volumes indicate virtually no changes to Cu-RTH before and after aging. Thus, assessments of long-range structural features by XRD and micropore volume after Cu-zeolites have been hydrothermally aged cannot be used as accurate predictors of SCR catalytic behavior.

Hydrothermal aging treatments did not affect the apparent activation energies on either Cu-AEI ($46\text{--}49\text{ kJ mol}^{-1}$) or Cu-CHA ($51\text{--}56\text{ kJ mol}^{-1}$), nor the apparent NO (0.5), O_2 (0.4) and NH_3 (~ 0) orders on Cu-AEI and the apparent NO (0.4–0.5) and O_2 (0.4–0.6) orders on Cu-CHA (Table 3). The apparent NH_3 order measured on Cu-CHA (-0.5) became less negative after hydrothermal aging (-0.1 , Table 3); we surmise that structural changes caused by hydrothermal aging and exposure to SCR gases led to a change in operation to a new kinetic regime characterized by weaker NH_3 inhibition. Turn-over rates were similar between the hydrothermally-aged Cu-CHA and Cu-AEI samples ($1.9\text{--}2.2 \times 10^{-3}$ mol NO (mol Cu) $^{-1}$

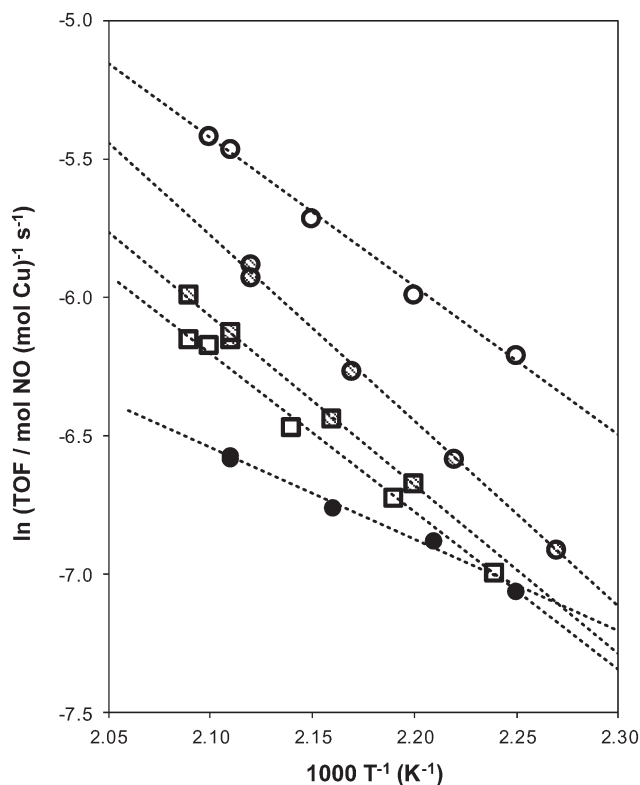


Fig. 4 Dependence of standard SCR turnover rates (per Cu) on temperature for fresh (circles) and aged (squares) Cu-form AEI (hollow), CHA (cross hatched), and RTH (filled circles) zeolites.

s^{-1}) and the apparent reaction orders and activation energies were identical for both samples (Table 3), providing evidence that these rate data were measured in equivalent kinetic regimes. These data indicate that the Cu species that remain active on both CHA and AEI after hydrothermal aging behave catalytically similar, which may be linked to the nature of the Cu^{2+} exchange sites at the 6-MR windows of D6R composite building units that are found in both CHA and AEI.

3.6. Characterization of Cu-form zeolites before and after hydrothermal aging, and after exposure to NO_x SCR

Ar adsorption isotherms (87 K) and micropore volumes (Fig. 6, Table 3) of Cu-zeolites after hydrothermal aging were indistinguishable before and after exposure to low temperature standard SCR reaction conditions (473 K). XRD patterns were also similar for hydrothermally-aged Cu-zeolites before and after exposure to standard SCR gases (Fig. 5). These characterization data indicate that further structural changes to the zeolite framework did not occur when aged Cu-zeolites were exposed to standard SCR gas mixtures. The number of H^+ sites on hydrothermally-aged Cu-AEI and Cu-CHA zeolites were also similar before and after exposure to standard SCR gas mixtures (Table 3), but H^+ sites were no longer detectable ($<0.03 H^+/Al$, Table 3) on hydrothermally-aged Cu-RTH exposed to SCR gases. UV-vis spectra of hydrothermally-aged Cu-CHA and Cu-RTH zeolites after exposure to standard SCR

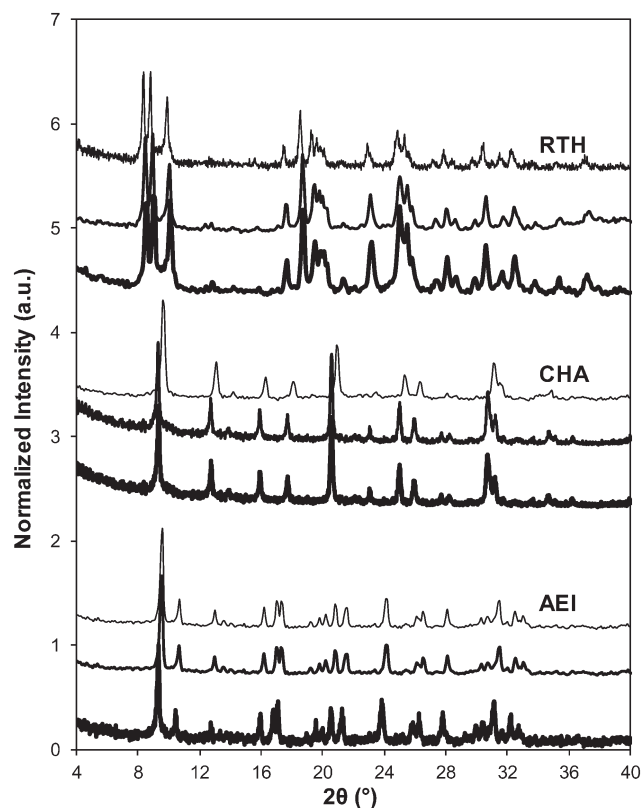


Fig. 5 Powder XRD patterns of fresh Cu-form before SCR (dark), aged Cu-form before SCR (medium), and aged Cu-form after SCR (light) on AEI, CHA, and RTH zeolites. Diffraction patterns are normalized so that the maximum peak intensity in each pattern is unity, and offset for clarity.

reactants (Fig. 3) showed a reduction in Cu^{2+} d-d transition intensity ($\sim 12\,500\text{ cm}^{-1}$) and concomitant increases in intensity for broad absorption bands between $20\,000\text{--}40\,000\text{ cm}^{-1}$. The spectra of Cu-AEI, however, retained similar d-d transition intensity after aging and exposure to SCR reactants, with an increase in intensity in the metal-ligand charge transfer region ($35\,000\text{--}47\,000\text{ cm}^{-1}$) that is also observed for Cu-CHA, but not for Cu-RTH.

The Cu structure in Cu-CHA, Cu-AEI and Cu-RTH, characterized by UV-vis spectra, showed hardly any changes after hydrothermal aging treatments, but showed noticeable decreases in Cu^{2+} intensity upon subsequent exposure to low temperature SCR reaction conditions. These findings provide evidence that hydrothermal aging causes removal of Al from framework to extraframework positions, and that further structural changes continue to occur in the presence of SCR reactants at low temperatures (473 K) because NH_3 facilitates the solvation and mobility of Cu cations.⁴² We speculate that an inactive copper aluminate phase ($CuAl_xO_y$) forms as a result of interactions of active Cu sites with extraframework $Al(OH)_3$ species, as proposed previously.^{14,17,35} UV-vis spectra of hydrothermally-aged Cu-RTH reveal decreased intensities for hydrated Cu^{2+} d-d transitions along with increases in new charge transfer bands between $20\,000\text{--}40\,000\text{ cm}^{-1}$ that may

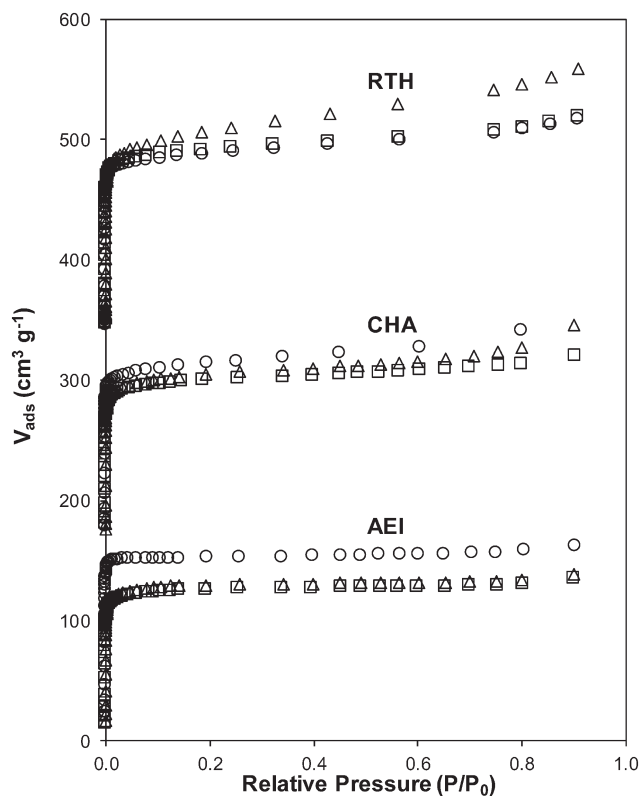


Fig. 6 Ar adsorption isotherms (87 K) on fresh Cu-form before SCR (circles), aged Cu-form before SCR (triangles), aged Cu-form after SCR (squares) on AEI, CHA, and RTH zeolites. Isotherms are vertically offset for clarity (CHA: $160 \text{ cm}^3 \text{ g}^{-1}$, RTH: by $320 \text{ cm}^3 \text{ g}^{-1}$).

reflect CuAl_xO_y species and account for decreases in SCR rate. Interestingly, any remaining H^+ sites in Cu-RTH upon hydrothermal aging and subsequent exposure to standard SCR reactants become inaccessible to NH_3 , suggesting that Cu active sites in RTH, which appear to catalyze SCR in a diffusion-limited regime before hydrothermal aging, also become inaccessible to SCR reactants after hydrothermal aging.

4. Conclusions

CHA and AEI zeolites are similar in structure, with three-dimensional micropore systems connected by symmetric 8-MR windows (0.38 nm diameter), while the RTH framework is a two-dimensional pore system with constrained, asymmetric 8-MR windows (0.56 nm \times 0.25 nm) that limit access in one dimension and effectively causes the RTH framework to behave as a one-dimensional pore system for NO_x SCR with NH_3 . As a result, standard SCR turnover rates (per Cu, 473 K) and apparent activation energies are similar between Cu-CHA and Cu-AEI, but turnover rates are lower (by $\sim 2\text{--}3\times$) and apparent activation energies are lower (by $\sim 2\times$) on Cu-RTH. Hydrothermal aging causes dealumination of Cu-CHA, Cu-AEI and Cu-RTH, evident in a decrease in the fraction of Al_f determined from ^{27}Al MAS NMR spectra and corresponding decreases in the number of H^+ sites quantified by NH_3 TPD, but does not cause noticeable changes in the bulk framework

structure assessed by XRD and micropore volume or in the Cu structure by UV-vis spectroscopy. The number of active Cu sites, however, decreased after hydrothermally aged samples were subsequently exposed to low temperature standard SCR reactants, evident in changes to UV-vis spectra and concomitant decreases in standard SCR turnover rates. Hydrothermal aging causes removal of Al from framework to extraframework positions, and further structural changes continue to occur in the presence of ammonia at low temperatures (473 K), which solvate and mobilize extraframework cations to facilitate the formation of inactive copper-aluminate phases (CuAl_xO_y). These structural changes appear to occur more readily in Cu-RTH than either Cu-AEI or Cu-CHA, providing further evidence linking the presence of double six-membered rings (D6R) in small-pore molecular sieve frameworks to increased resistance to active site and framework structural changes upon hydrothermal aging.

Bulk structural characterization of small-pore zeolites after hydrothermal aging treatments cannot be used to accurately infer catalytic behavior for low temperature NO_x SCR with NH_3 . This is evident in the case of hydrothermally-aged Cu-RTH, which deactivates completely upon exposure to standard SCR reactants but is characterized by similar bulk properties (XRD, micropore volume) before and after hydrothermal aging. Probes of Al structure (e.g., ^{27}Al MAS NMR) reveal that octahedrally-coordinated Al species are formed after hydrothermal aging of Cu-zeolites, but in amounts that are unable to account for the much larger disappearance in Brønsted acid sites titrated by NH_3 , providing another reminder that methods to directly probe active sites are needed to assess their structural changes. We conclude that more accurate assessments of molecular sieve framework topologies that are viable for practical NO_x SCR catalysis require quantification and characterization of Al and Cu site structures after hydrothermally aged samples are exposed to low temperature SCR reaction conditions. We expect that holistic approaches to active site characterization, especially of Al and Cu sites, in Cu-zeolites after hydrothermal aging and subsequent exposure to low temperature SCR reaction conditions will be able to provide more accurate guidance about molecular sieve topologies that are viable candidates for practical SCR technologies.

Acknowledgements

We acknowledge the financial support provided by the National Science Foundation GOALI program under award number 1258715-CBET. RG acknowledges the financial support from a Ralph E. Powe Junior Faculty Enhancement Award from the Oak Ridge Associated Universities (ORAU). MD acknowledges Research Foundation Flanders (FWO) for post-doctoral funding. We thank Dr. John Harwood (Purdue Interdepartmental NMR Facility) for assistance collecting the NMR spectra, and Dr. Atish A. Parekh for helpful technical discussions. We also thank Daniel Gonzalez (Universidad Nacional de Colombia), through the Undergraduate Research

Experience Purdue-Colombia (UREP-C) program, for experimental assistance constructing the apparatus to perform hydrothermal aging treatments and performing some aging experiments on CHA zeolites. We also thank Sachem, Inc. for providing the organic structure-directing agent used to synthesize SSZ-13.

References

- 1 S. Brandenberger, O. Kröcher, A. Tissler and R. Althoff, *Catal. Rev.: Sci. Eng.*, 2008, **50**, 492–531.
- 2 T. Komatsu, M. Nunokawa, I. S. Moon, T. Takahara, S. Namba and T. Yashima, *J. Catal.*, 1994, **148**, 427–437.
- 3 G. Delahay, S. Kieger, N. Tanchoux, P. Trens and B. Coq, *Appl. Catal., B*, 2004, **52**, 251–257.
- 4 G. Delahay, E. A. Villagomez, J.-M. Ducere, D. Berthomieu, A. Goursot and B. Coq, *ChemPhysChem*, 2002, **3**, 686–692.
- 5 J. H. Baik, S. D. Yim, I.-S. Nam, Y. S. Mok, J.-H. Lee, B. K. Cho and S. H. Oh, *Top. Catal.*, 2004, **30**, 37–41.
- 6 J.-H. Park, H. J. Park, J. H. Baik, I.-S. Nam, C.-H. Shin, J.-H. Lee, B. K. Cho and S. H. Oh, *J. Catal.*, 2006, **240**, 47–57.
- 7 K. Kamasamudram, N. W. Currier and X. Chen, *Catal. Today*, 2010, **151**, 212–222.
- 8 J. H. Kwak, R. G. Tonkyn, D. H. Kim, J. Szanyi and C. H. F. Peden, *J. Catal.*, 2010, **275**, 187–190.
- 9 S. T. Korhonen, D. W. Fickel, R. F. Lobo, B. M. Weckhuysen and A. M. Beale, *Chem. Commun.*, 2011, **47**, 800–802.
- 10 A. M. Beale, F. Gao, I. Lezcano-Gonzalez, C. H. F. Peden and J. Szanyi, *Chem. Soc. Rev.*, 2015, **44**, 7371–7405.
- 11 K. Rahkamaa-Tolonen, T. Maunula, M. Lomma, M. Huuhtanen and R. L. Keiski, *Catal. Today*, 2005, **100**, 217–222.
- 12 Q. Ye, L. Wang and R. T. Yang, *Appl. Catal., A*, 2012, **427**, 24–34.
- 13 D. W. Fickel, E. D'Addio, J. A. Lauterbach and R. F. Lobo, *Appl. Catal., B*, 2011, **102**, 441–448.
- 14 J. H. Kwak, D. Tran, S. D. Burton, J. Szanyi, J. H. Lee and C. H. F. Peden, *J. Catal.*, 2012, **287**, 203–209.
- 15 K. C. C. Kharas, H. J. Robota and D. J. Liu, *Appl. Catal., B*, 1993, **2**, 225–237.
- 16 S. A. Gómez, A. Campero, A. Martínez-Hernández and G. A. Fuentes, *Appl. Catal., A*, 2000, **197**, 157–164.
- 17 P. G. Blakeman, E. M. Burkholder, H. Y. Chen, J. E. Collier, J. M. Fedeyko, H. Jobson and R. R. Rajaram, *Catal. Today*, 2014, **231**, 56–63.
- 18 S. Shwan, R. Nedyalkova, J. Jansson, J. Korsgren, L. Olsson and M. Skoglundh, *Ind. Eng. Chem. Res.*, 2012, **51**, 12762–12772.
- 19 P. J. Andersen, J. E. Bailie, J. L. Casci, H. Y. Chen, J. M. Fedeyko, R. K. Shin Foo and R. R. Rajaram, *US Pat.*, 0290963, 2010.
- 20 I. Bull, R. S. Boorse, W. M. Jaglowski, G. S. Koermer, A. Moini, J. A. Patchett, W. Xue, P. Burk, J. C. Dettling and M. T. Caudle, *US Pat.*, 0226545, 2008.
- 21 M. Moliner, C. Franch, E. Palomares, M. Grill and A. Corma, *Chem. Commun.*, 2012, **48**, 8264–8266.
- 22 A. Lorena Picone, S. J. Warrender, A. M. Z. Slawin, D. M. Dawson, S. E. Ashbrook, P. A. Wright, S. P. Thompson, L. Gaberova, P. L. Llewellyn, B. Moulin, A. Vimont, M. Daturi, M. B. Park, S. K. Sung, I.-S. Nam and S. B. Hong, *Microporous Mesoporous Mater.*, 2011, **146**, 36–47.
- 23 D. Xie, L. B. McCusker, C. Baerlocher, S. I. Zones, W. Wan and X. Zou, *J. Am. Chem. Soc.*, 2013, **135**, 10519–10524.
- 24 T. M. Davis, A. T. Liu, C. M. Lew, D. Xie, A. I. Benin, S. Elomari, S. I. Zones and M. W. Deem, *Chem. Mater.*, 2016, **28**, 708–711.
- 25 D. Jo, J. Bin Lim, T. Ryu, I.-S. Nam, M. A. Cambor and S. B. Hong, *J. Mater. Chem. A*, 2015, **3**, 19322–19329.
- 26 S. Altwasser, J. Jiao, S. Steuernagel, J. Weitkamp and M. Hunger, *Stud. Surf. Sci. Catal.*, 2004, **154B**, 1212–1213.
- 27 M. Nielsen, R. Y. Brogaard, H. Falsig, P. Beato, O. Swang and S. Svelle, *ACS Catal.*, 2015, **5**, 7131–7139.
- 28 K. Ehrhardt, M. Suckow and W. Lutz, *Stud. Surf. Sci. Catal.*, 1995, **94**, 179–186.
- 29 L. Ma, Y. Cheng, G. Cavataio, R. W. McCabe, L. Fu and J. Li, *Appl. Catal., B*, 2014, **156–157**, 428–437.
- 30 M. V. L. Pereira, A. Nicolle and D. Berthout, *Catal. Today*, 2015, **258**, 424–431.
- 31 L. R. Aramburo, L. Karwacki, P. Cubillas, S. Asahina, D. A. M. de Winter, M. R. Drury, I. L. C. Buurmans, E. Stavitski, D. Mores, M. Daturi, P. Bazin, P. Dumas, F. Thibault-Starzyk, J. A. Post, M. W. Anderson, O. Terasaki and B. M. Weckhuysen, *Chem. – Eur. J.*, 2011, **17**, 13773–13781.
- 32 D. Wang, Y. Jangjou, Y. Liu, M. K. Sharma, J. Luo, J. Li, K. Kamasamudram and W. S. Epling, *Appl. Catal., B*, 2015, **165**, 438–445.
- 33 J. Wang, Z. Peng, H. Qiao, L. Han, W. Bao, L. Chang, G. Feng and W. Liu, *RSC Adv.*, 2014, **4**, 42403–42411.
- 34 S. J. Schmieg, S. H. Oh, C. H. Kim, D. B. Brown, J. H. Lee, C. H. F. Peden and D. H. Kim, *Catal. Today*, 2012, **184**, 252–261.
- 35 W. Su, Z. Li, Y. Peng and J. Li, *Phys. Chem. Chem. Phys.*, 2015, **17**, 29142–29149.
- 36 M. Dusselier, M. A. Deimund, J. E. Schmidt and M. E. Davis, *ACS Catal.*, 2015, **5**, 6078–6085.
- 37 F. Gao, Y. Wang, N. M. Washton, M. Kollar, J. Szanyi and C. H. F. Peden, *ACS Catal.*, 2015, **5**, 6780–6791.
- 38 A. V. Kucherov and A. A. Slinkin, *Zeolites*, 1986, **6**, 175–180.
- 39 G. T. Kerr, *J. Phys. Chem.*, 1967, **71**, 4155–4156.
- 40 G. T. Kerr, *J. Catal.*, 1969, **15**, 200–204.
- 41 M. C. Silaghi, C. Chizallet, E. Petracovschi, T. Kerber, J. Sauer and P. Raybaud, *ACS Catal.*, 2015, **5**, 11–15.
- 42 C. Paolucci, A. A. Parekh, I. Khurana, J. R. Di Iorio, H. Li, J. D. Albarracin Caballero, A. Shih, T. Anggara, W. N. Delgass, J. T. Miller, F. H. Ribeiro, R. Gounder and W. F. Schneider, *J. Am. Chem. Soc.*, 2016, **138**, 6028–6048.
- 43 T. V. W. Janssens, H. Falsig, L. F. Lundegaard, P. N. R. Vennestrom, S. Rasmussen, P. G. Moses, F. Giordanino, E. Borfecchia, K. A. Lomachenko, C. Lamberti, S. Bordiga, A. Godiksen, S. Mossin and P. Beato, *ACS Catal.*, 2015, **5**, 2832–2845.

- 44 F. Gao, N. M. Washton, Y. Wang, M. Kollár, J. Szanyi and C. H. F. Peden, *J. Catal.*, 2015, **331**, 25–38.
- 45 S. A. Bates, A. A. Verma, C. Paolucci, A. A. Parekh, T. Anggara, A. Yezerets, W. F. Schneider, J. T. Miller, W. N. Delgass and F. H. Ribeiro, *J. Catal.*, 2014, **312**, 87–97.
- 46 S. I. Zones, *US Pat.*, 4544538A, 1985.
- 47 M. Dusselier, J. E. Schmidt, R. Moulton, B. Haymore, M. Hellums and M. E. Davis, *Chem. Mater.*, 2015, **27**, 2695–2702.
- 48 J. E. Schmidt, M. A. Deimund, D. Xie and M. E. Davis, *Chem. Mater.*, 2015, **27**, 3756–3762.
- 49 J. E. Schmidt, M. W. Deem and M. E. Davis, *Angew. Chem., Int. Ed.*, 2014, **53**, 8372–8374.
- 50 J. E. Schmidt, M. A. Deimund and M. E. Davis, *Chem. Mater.*, 2014, **34**, 7774–7779.
- 51 C. Baerlocher, W. H. Baur, J. M. Bennett, H. Gies, J. B. Higgins, R. Kirchner and D. H. Olson, *Zeolites*, 1996, **17**, 1–230.
- 52 S. A. Bates, A. A. Verma, C. Paolucci, A. A. Parekh, T. Anggara, A. Yezerets, W. F. Schneider, J. T. Miller, W. N. Delgass and F. H. Ribeiro, *J. Catal.*, 2014, **312**, 87–97.
- 53 J. R. Di Iorio, S. A. Bates, A. A. Verma, W. N. Delgass, F. H. Ribeiro, J. T. Miller and R. Gounder, *Top. Catal.*, 2015, **58**, 424–434.
- 54 S. I. Zones, Y. Nakagawa, S. T. Evans and G. S. Lee, *US Pat.*, 5958370A, 1999.
- 55 G. S. Lee and S. I. Zones, *US Pat.*, 6605267B1, 2003.
- 56 G. Centi and S. Perathoner, *Appl. Catal., A*, 1995, **132**, 179–259.
- 57 R. Gounder, A. J. Jones, R. T. Carr and E. Iglesia, *J. Catal.*, 2012, **286**, 214–223.
- 58 A. I. Biaglow, D. J. Parrillo, G. T. Kokotailo and R. J. Gorte, *J. Catal.*, 1994, **148**, 213–223.
- 59 S. A. Bates, W. N. Delgass, F. H. Ribeiro, J. T. Miller and R. Gounder, *J. Catal.*, 2014, **312**, 26–36.
- 60 J. R. Di Iorio and R. Gounder, *Chem. Mater.*, 2016, **28**, 2236–2247.
- 61 C. Paolucci, J. R. Di Iorio, F. H. Ribeiro, R. Gounder and W. F. Schneider, *Adv. Catal.*, 2016, **59**, 1–107.
- 62 J. Texter, D. H. Strome, R. G. Herman and K. Klier, *J. Phys. Chem.*, 1977, **81**, 333–338.
- 63 F. Giordanino, P. N. R. Vennestrom, L. F. Lundegaard, F. N. Stappen, S. Mossin, P. Beato, S. Bordiga and C. Lamberti, *Dalton Trans.*, 2013, **42**, 12741–12761.
- 64 K. L. Fajdala, I. J. Drake, A. T. Bell and T. D. Tilley, *J. Am. Chem. Soc.*, 2004, **126**, 10864–10866.
- 65 J. A. van Bokhoven, A. L. Roest, D. C. Koningsberger, J. T. Miller, G. H. Nachttegaal and A. P. M. Kentgens, *J. Phys. Chem. B*, 2000, **104**, 6743–6754.
- 66 A. I. Biaglow, D. J. Parrillo, G. T. Kokotailo and R. J. Gorte, *J. Catal.*, 1994, **148**, 213–223.
- 67 R. Gounder and E. Iglesia, *J. Catal.*, 2011, **277**, 36–45.
- 68 M. D. Foster, I. Rivin, M. M. J. Treacy and O. D. Friedrichs, *Microporous Mesoporous Mater.*, 2006, **90**, 32–38.